Spectrochimica Acta Part A: Molecular and Biomolecular Spectroscopy 245 (2021) 118906

Contents lists available at ScienceDirect

Spectrochimica Acta Part A: Molecular and Biomolecular Spectroscopy

journal homepage: www.elsevier.com/locate/saa

The structure-Raman spectra relationships of $Mg_3(PO_4)_2$ polymorphs: A comprehensive experimental and DFT study

Xin Hu [a,b], Lei Liu [c], Shuangmeng Zhai [a,*]

[a] Key Laboratory of High-temperature and High-pressure Study of the Earth's Interior, Institute of Geochemistry, Chinese Academy of Sciences, Guiyang 550081, Guizhou, China
[b] University of Chinese Academy of Sciences, Beijing 100049, China
[c] United Laboratory of High-Pressure Physics and Earthquake Science, Institute of Earthquake Forecasting, China Earthquake Administration, Beijing 100036, China

ARTICLE INFO

Article history:
Received 8 July 2020
Received in revised form 24 August 2020
Accepted 29 August 2020
Available online 3 September 2020

Keywords:
$Mg_3(PO_4)_2$
Raman spectroscopy
DFT calculation

ABSTRACT

Three $Mg_3(PO_4)_2$ polymorphs ($Mg_3(PO_4)_2$-I, II, III) were synthesized at high-pressure and high-temperature conditions. The structures and vibrational properties of $Mg_3(PO_4)_2$ polymorphs were studied by X-ray diffraction (XRD), Raman spectroscopy, and density functional theory (DFT) calculations. The obvious different P—O stretching vibrational modes were experimentally observed for $Mg_3(PO_4)_2$-I, II, III. The calculated vibrational frequencies were in good agreement with measurements. All the observed vibrational modes for $Mg_3(PO_4)_2$-I, II, III were well assigned based on the calculations, which provided a support for investigating and comparing vibrational properties of three $Mg_3(PO_4)_2$ polymorphs.

1. Introduction

$Mg_3(PO_4)_2$ has three common polymorphs: $Mg_3(PO_4)_2$-I, II, III. $Mg_3(PO_4)_2$-II and $Mg_3(PO_4)_2$-III can be obtained from $Mg_3(PO_4)_2$-I at high-pressure and high-temperature conditions [1–6]. $Mg_3(PO_4)_2$-I (farringtonite) has been found in meteorites coexisting with olivine, which is considered as a unique mineral in meteorites and lunar rocks [7]. The presence of $Mg_3(PO_4)_2$ in the composition of urinary calculi indicates that it has good biocompatibility [8], which has attracted interest as a biomaterial for hard tissue implants [9,10]. $Mg_3(PO_4)_2$-I powder was found to be suitable for 3D printing of hard tissue implants, and biomedical behavior of magnesium alloys can also be improved by regulating the content of $Mg_3(PO_4)_2$ compounds [11,12]. Moreover, due to its special physical and chemical properties, $Mg_3(PO_4)_2$-I has been the subjects of many studies. $Mg_3(PO_4)_2$-I was found to be able to adsorb heavy ions from solution through the ion replacement mechanism, which is widely used as active component for nutrients removal from swine wastewater [13,14]. Owning to its excellent chemical and thermal stability, the pervasion of $Mg_3(PO_4)_2$-I not only improves the performance and life of lithium batteries, but also has protective effects against the imperfect expansion coefficient and mechanical properties of ceramics [15,16]. The applications of $Mg_3(PO_4)_2$-I have been widely studied, but the physical and chemical properties of $Mg_3(PO_4)_2$-II and $Mg_3(PO_4)_2$-III are scarcely explored. The understanding of the structure and vibrational properties is essential for performance.

The physical and chemical properties of a compound are closely related to its structure. The crystal structures of $Mg_3(PO_4)_2$-I and $Mg_3(PO_4)_2$-II are well determined by XRD, which belong to the $P\,2_1/n$ space group [1–4,7,17–19]. Burnet et al. reported the structure of $Mg_3(PO_4)_2$-III [4,5], which belongs to $P\text{-}1$ space group. The crystal structures of $Mg_3(PO_4)_2$-I, II, III are illustrated in Fig. 1. $Mg_3(PO_4)_2$-I consists of one distorted six-coordinated Mg(2) and two distinct five-coordinate Mg (1) cations. In the crystal of $Mg_3(PO_4)_2$-II, Mg(1) and Mg(2) atoms are coordinate to six oxygen atoms, and the $Mg(1)O_6$ group and $Mg(2)O_6$ share four O atoms of type O (2) and O (4). The Mg atoms in $Mg_3(PO_4)_2$-III exhibit a wide range of coordination numbers, the coordinated number for Mg(1), Mg(2) and Mg(3) are 5, 5 and 4, while the Mg(4), Mg(5) and Mg(6) atoms coordinate to six oxygen atoms. More intricately, there are four different PO_4 tetrahedra in $Mg_3(PO_4)_2$-III.

Raman spectroscopy is a cogent tool for studying structural properties of chemical systems. Raman spectra of $Mg_3(PO_4)_2$-I are reported in some previous studies [18,20]. However, the Raman spectra of $Mg_3(PO_4)_2$-II and $Mg_3(PO_4)_2$-III have not been reported. On the other hand, $Mg_3(PO_4)_2$-I and $Mg_3(PO_4)_2$-II are suitable to study the relationship between vibrational modes (Raman spectra) and chemical bonds (P—O) since the influence of chemical components and space group can be excluded. By comparing the Raman of $Mg_3(PO_4)_2$-I, II, III, the vibrational properties of structural transformation are easy to be understood.

An effective theoretical analysis is a key way to obtain accurate Raman band and structural relationship. Various authors report the connection between Raman band and structure of compound through DFT calculations [21–23]. In this work, the experimentally

* Corresponding author.
E-mail address: zhaishuangmeng@mail.gyig.ac.cn (S. Zhai).

https://doi.org/10.1016/j.saa.2020.118906
1386-1425/

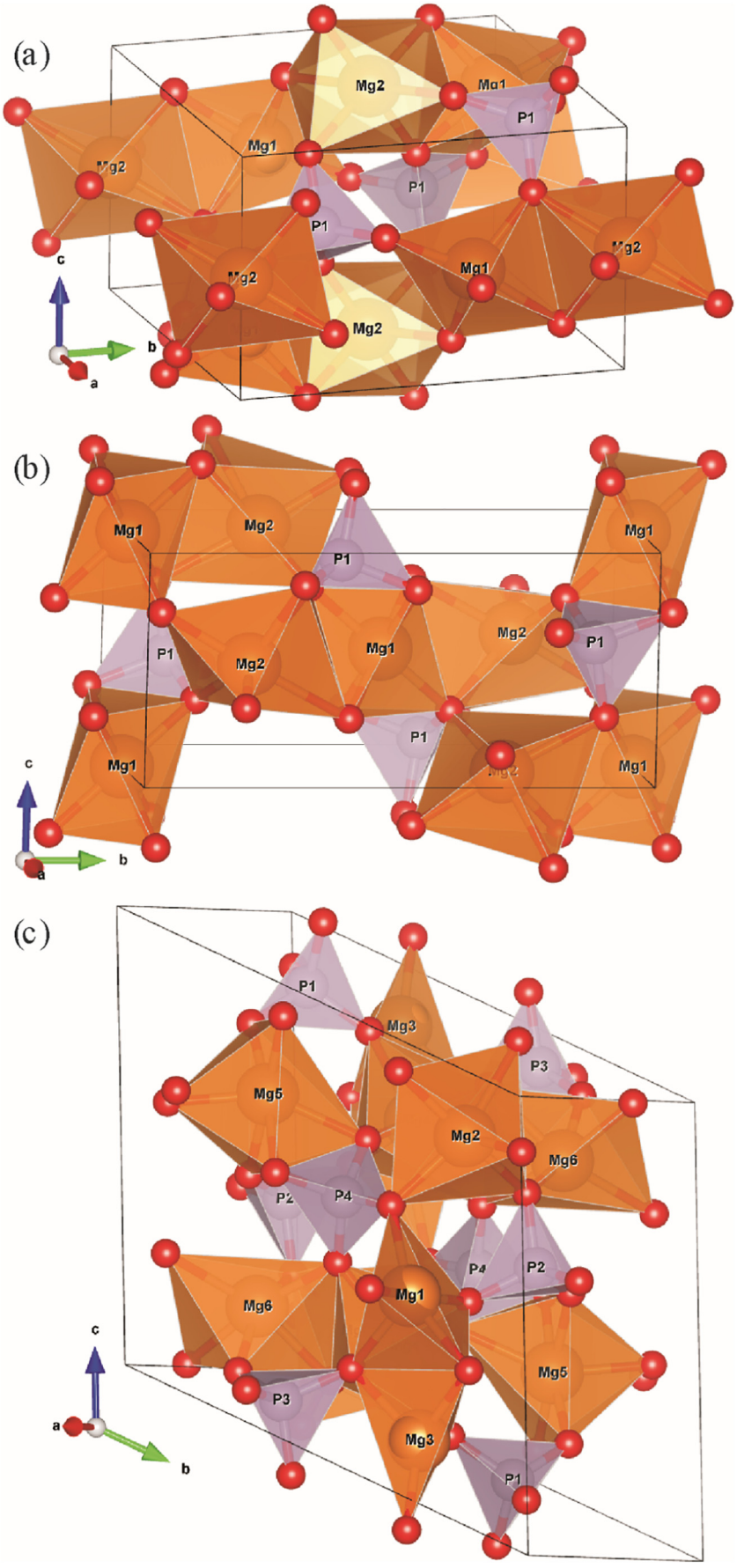

Fig. 1. The crystal structures of three $Mg_3(PO_4)_2$ polymorphs. (a) $Mg_3(PO_4)_2$-I, (b) $Mg_3(PO_4)_2$-II, (c) $Mg_3(PO_4)_2$-III.

measured Raman spectra and DFT calculations were obtained to study the effect of structural transformations on vibrational properties between $Mg_3(PO_4)_2$-I, II, III. The difference of experimental and calculated spectra was explained based on details of crystal structures. The observed vibrational modes of $Mg_3(PO_4)_2$-I, II, III were indexed according to the calculations.

2. Experimental and computational details

2.1. Experimental details

$Mg_3(PO_4)_2$-I polycrystalline powder was synthesized through a solid-state reaction, and the procedure is similar to previous studies [1–6]. Analytical MgO and $NH_4H_2PO_4$ were weighted at molar ratio of 3:2 and ground thoroughly in an agate mortar and then compressed into pellets with a diameter of 10 mm. After pre-heating at 773 K for 12 h, the pellets were ground thoroughly again and heated to 1173 K for 72 h for obtaining pure $Mg_3(PO_4)_2$-I phase. Pure $Mg_3(PO_4)_2$-II was obtained at 1.6 GPa and 1173 K for 48 h by using $Mg_3(PO_4)_2$-I as the starting materials. Similarly, pure $Mg_3(PO_4)_2$-III was synthesized by using obtained $Mg_3(PO_4)_2$-I as the starting material at 2.2 GPa and 1323 K for 66 h.

2.2. XRD and Raman spectroscopic characterization

The XRD patterns of $Mg_3(PO_4)_2$-I, II, III were collected by using an Empyrean diffractometer with Cu K_α radiation operated at 40 kV and 200 mA. The collected XRD patterns of $Mg_3(PO_4)_2$-I, II, III were refined using EXPGUI/GSAS to obtain lattice parameters and structural information [24,25].

The Raman spectra of samples at ambient conditions were measured by a Horiba LabRam HR Evolution Raman spectrometer equipped with an 1800 g/mm grating. A pulsed YAG: Nd^{3+} laser with a wavelength of 532 nm and a power of 100 mW was used as the excitation source. The acquisition time of Raman spectra was 80 s. The resolution of the Raman spectra is 1 cm^{-1}. All the Raman spectra were analyzed by using the PeakFit program (SPSS Inc., Chicago) to get reasonable approximations.

2.3. Computational methods

The Raman properties calculation were performed by density functional theory (DFT) and density functional perturbation theory (DFPT) as implemented in the CASTEP code [26–30]. The functional set GGA (PBE) version with optimized norm-conserving pseudopotentials was used [31–34]. Broyden-Fletcher-Goldfarb-Shanno optimization scheme with a convergence threshold on displacement of 0.002 Å was used for geometry optimization. A $2 \times 2 \times 2$ Monkhorst-Pack grid of k points was adopted for sampling the Brillouin zone [35,36].

The total-energy convergence criterion of 2×10^{-5} eV/atom was used in the self-consistent field calculations. The convergence threshold on atomic forces of 0.05 eV/Å. Because of the different crystal symmetry $Mg_3(PO_4)_2$-III, $Mg_3(PO_4)_2$-I and $Mg_3(PO_4)_2$-II, the energy cutoff for the plane-wave basis was chosen to be 770 eV, 680 eV and 789.1 eV, respectively.

The difference between the calculated and experimental Raman shifts for $Mg_3(PO_4)_2$ polymorphs indeed exists. The calculated Raman spectrum was calibrated using a scaling factor to match the experimental Raman spectrum. In this case, the scaling factor is the ratio of Raman shifts of the most intensive peaks in experimental and calculated Raman spectra. In the present study, the scaling factors for $Mg_3(PO_4)_2$-I, II, III are 1.050, 1.055 and 1.070, respectively. The method of correcting calculated Raman shifts has been widely used in many studies [37–39].

3. Results and discussion

3.1. XRD and structure

The measured and refined XRD patterns of $Mg_3(PO_4)_2$-I, II, III are reproduced in Fig. 2. All characteristic peaks of $Mg_3(PO_4)_2$ compounds demonstrate that they are pure phases.

The refined and corresponding calculated unit cell parameters of $Mg_3(PO_4)_2$-I, II, III are given in Table 1. Those experimental parameters are similar with previous studies on $Mg_3(PO_4)_2$-I, II, III [1–5,7,17–19]. The atomic positions of optimized $Mg_3(PO_4)_2$-I, II, III are listed in Appendix A in Support Information.

It is noted that the P—O bond lengths and O-P-O bond angles of $Mg_3(PO_4)_2$-II are more scattering than those of $Mg_3(PO_4)_2$-I. Moreover, the averaged P—O bond length of $Mg_3(PO_4)_2$-II is shorter than those of $Mg_3(PO_4)_2$-I. Compared with $Mg_3(PO_4)_2$-II, the structural transformation increases the number of PO_4 tetrahedra in $Mg_3(PO_4)_2$-III. The selected information is given in Tables 2 and 3.

3.2. Raman spectroscopy study

Raman spectroscopy is convenient and powerful tool to study structural characters of materials through the vibration and rotation of molecular bonds. It provides more valuable information on microscale analysis than XRD, especially for $Mg_3(PO_4)_2$-I and $Mg_3(PO_4)_2$-II crystals

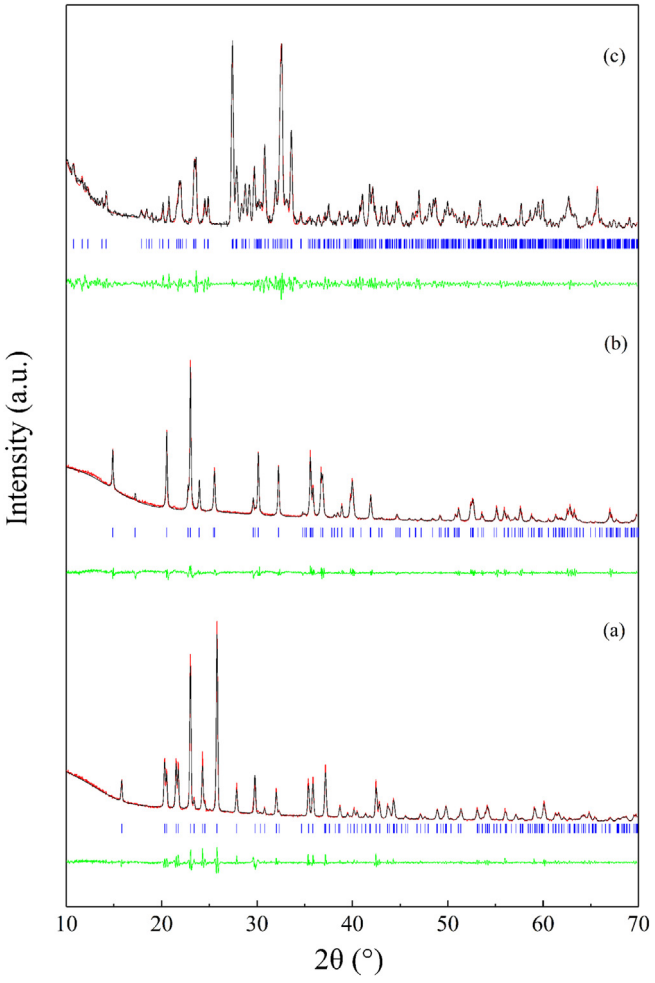

Fig. 2. Rietveld XRD patterns of $Mg_3(PO_4)_2$ polymorphs: experimental pattern (black line), calculated data (red line), positions of Bragg reflections (blue pot). The lower green curve is the difference profile. (a) $Mg_3(PO_4)_2$-I, (b) $Mg_3(PO_4)_2$-II, (c) $Mg_3(PO_4)_2$-III.

Table 1
The unit cell parameters of $Mg_3(PO_4)_2$ polymorphs in the present study.

Parameters	a (Å)	b (Å)	c (Å)	α (°)	β (°)	γ (°)	V(Å^3)
Exp. $Mg_3(PO_4)_2$-I	7.5928(4)	8.2285 (4)	5.0694(27)	90	94.121(3)	90	315.91
Cal. $Mg_3(PO_4)_2$-I	7.8402	8.4487	5.1102	90	93.744	90	337.77
Exp. $Mg_3(PO_4)_2$-II	5.9001(2)	10.2033 (4)	4.7345(2)	90	90	90.664(3)	285.00
Cal. $Mg_3(PO_4)_2$-II	6.2144	10.5101	4.8973	90	90	88.1767	319.70
Exp. $Mg_3(PO_4)_2$-III	8.5151(12)	8.9979(12)	9.319(13)	116.039(5)	91.451(5)	114.524(4)	564.16
Cal. $Mg_3(PO_4)_2$-III	8.7055	9.1844	9.4829	116.005	91.191	114.429	601.21

Table 2
Refined and calculated P—O bonds length (Å) and angle (°) of $Mg_3(PO_4)_2$-I, II.

$Mg_3(PO_4)_2$-I				$Mg_3(PO_4)_2$-II			
Refined		Calculated		Refined		Calculated	
$P\text{-}O_1$	1.53321(7)	$P\text{-}O_1$	1.52749	$P\text{-}O_1$	1.54148(6)	$P\text{-}O_1$	1.52412
$P\text{-}O_2$	1.50677(7)	$P\text{-}O_2$	1.52380	$P\text{-}O_2$	1.64602(5)	$P\text{-}O_2$	1.57840
$P\text{-}O_3$	1.53476(7)	$P\text{-}O_3$	1.53782	$P\text{-}O_3$	1.45102(5)	$P\text{-}O_3$	1.52946
$P\text{-}O_4$	1.52756(6)	$P\text{-}O_4$	1.53696	$P\text{-}O_4$	1.43341(4)	$P\text{-}O_4$	1.52335
$O_1\text{-}P\text{-}O_2$	111.710(4)	$O_1\text{-}P\text{-}O_2$	110.668	$O_1\text{-}P\text{-}O_2$	102.366(2)	$O_1\text{-}P\text{-}O_2$	103.268
$O_1\text{-}P\text{-}O_3$	103.760(2)	$O_1\text{-}P\text{-}O_3$	104.317	$O_1\text{-}P\text{-}O_3$	114.286(0)	$O_1\text{-}P\text{-}O_3$	111.935
$O_1\text{-}P\text{-}O_4$	110.398(3)	$O_1\text{-}P\text{-}O_4$	110.249	$O_1\text{-}P\text{-}O_4$	118.149(1)	$O_1\text{-}P\text{-}O_4$	112.017
$O_2\text{-}P\text{-}O_3$	112.075(2)	$O_2\text{-}P\text{-}O_3$	112.871	$O_2\text{-}P\text{-}O_3$	118.521(2)	$O_2\text{-}P\text{-}O_3$	112.824
$O_2\text{-}P\text{-}O_4$	108.668(3)	$O_2\text{-}P\text{-}O_4$	108.986	$O_2\text{-}P\text{-}O_4$	95.201(3)	$O_2\text{-}P\text{-}O_4$	103.336
$O_3\text{-}P\text{-}O_4$	110.178(3)	$O_3\text{-}P\text{-}O_4$	109.679	$O_3\text{-}P\text{-}O_4$	107.308(3)	$O_3\text{-}P\text{-}O_4$	112.751

with same chemical composition and space group. According to the factor group analysis based on the $P\,2_1/n$ space group and general point group $C2h$ (mmm) [40], both $Mg_3(PO_4)_2$-I and $Mg_3(PO_4)_2$-II have 36 Raman active vibrations:

$$\Gamma = 18\ A_g + 18\ B_g.$$

$Mg_3(PO_4)_2$-III is triclinic with space group *P -1* and has 78 Raman active vibrations [40]:

$$\Gamma = 78\ A_g.$$

Due to the decrease of symmetry, the B_g species of $Mg_3(PO_4)_2$-III is eliminated.

The experimental Raman spectrum of $Mg_3(PO_4)_2$-I collected at ambient conditions in the range of 100–1200 cm^{-1} is shown Fig. 3, together with calculated spectrum. Due to low intensity and/or overlapping of some bands, the observed vibrational modes are less than the predicted. Only 19 Raman active bands are observed for $Mg_3(PO_4)_2$-I. It should be noted that no Raman modes are observed in the range from 670 to 950 cm^{-1}, which is consistent with the calculated results. It is obvious that the observed Raman spectrum of $Mg_3(PO_4)_2$-I displays two intense band at 987 and 1029 cm^{-1} and their theoretical counterparts are at 983 and 1028 cm^{-1} which are attributed to the ν_1 symmetric stretching vibrations of PO_4 tetrahedra. Other Raman bands are observed at 1075, 1123 and 1145 cm^{-1}, and in the theoretical spectrum these bands appear at 1081, 1123 and 1142 cm^{-1}, which are assigned to the ν_3 antisymmetric stretching vibrations of PO_4 tetrahedra. The

Table 3
Refined and calculated P—O bonds length (Å) and angle (°) of $Mg_3(PO_4)_2$-III.

Refined							
$P_1\text{-}O_1$	1.52558(11)	$P_2\text{-}O_5$	1.52250(9)	$P_3\text{-}O_9$	1.51791(9)	$P_4\text{-}O_{13}$	1.52538(8)
$P_1\text{-}O_2$	1.52714(7)	$P_2\text{-}O_6$	1.52530(9)	$P_3\text{-}O_{10}$	1.53313(9)	$P_4\text{-}O_{14}$	1.52453(11)
$P_1\text{-}O_3$	1.54235(8)	$P_2\text{-}O_7$	1.53594(11)	$P_3\text{-}O_{11}$	1.54521(10)	$P_4\text{-}O_{15}$	1.54696(11)
$P_1\text{-}O_4$	1.56270(10)	$P_2\text{-}O_8$	1.53942(9)	$P_3\text{-}O_{12}$	1.56392(10)	$P_4\text{-}O_{16}$	1.54506(8)
$O_1\text{-}P_1\text{-}O_2$	110.938(4)	$O_5\text{-}P_2\text{-}O_6$	111.132(5)	$O_9\text{-}P_3\text{-}O_{10}$	112.934(5)	$O_{13}\text{-}P_3\text{-}O_{14}$	112.207(4)
$O_1\text{-}P_1\text{-}O_3$	110.126(4)	$O_5\text{-}P_2\text{-}O_7$	109.609(5)	$O_9\text{-}P_3\text{-}O_{11}$	109.466(5)	$O_{13}\text{-}P_3\text{-}O_{15}$	102.938(3)
$O_1\text{-}P_1\text{-}O_4$	104.568(5)	$O_5\text{-}P_2\text{-}O_8$	110.865(5)	$O_9\text{-}P_3\text{-}O_{12}$	111.813(5)	$O_{13}\text{-}P_3\text{-}O_{16}$	102.946(6)
$O_2\text{-}P_1\text{-}O_3$	110.063(4)	$O_6\text{-}P_2\text{-}O_7$	109.701(5)	$O_{10}\text{-}P_3\text{-}O_{11}$	105.699(3)	$O_{14}\text{-}P_3\text{-}O_{15}$	108.800(5)
$O_2\text{-}P_1\text{-}O_4$	116.030(5)	$O_6\text{-}P_2\text{-}O_8$	107.605(3)	$O_{10}\text{-}P_3\text{-}O_{12}$	106.897(5)	$O_{14}\text{-}P_3\text{-}O_{16}$	113.199(5)
$O_3\text{-}P_1\text{-}O_4$	104.796(4)	$O_7\text{-}P_2\text{-}O_8$	107.852(5)	$O_{11}\text{-}P_3\text{-}O_{12}$	109.817(5)	$O_{15}\text{-}P_3\text{-}O_{16}$	109.070(4)
Calculated							
$P_1\text{-}O_1$	1.55416	$P_2\text{-}O_5$	1.54874	$P_3\text{-}O_9$	1.54388	$P_4\text{-}O_{13}$	1.55586
$P_1\text{-}O_2$	1.55165	$P_2\text{-}O_6$	1.55561	$P_3\text{-}O_{10}$	1.55402	$P_4\text{-}O_{14}$	1.55452
$P_1\text{-}O_3$	1.56814	$P_2\text{-}O_7$	1.56249	$P_3\text{-}O_{11}$	1.56829	$P_4\text{-}O_{15}$	1.57242
$P_1\text{-}O_4$	1.59456	$P_2\text{-}O_8$	1.56453	$P_3\text{-}O_{12}$	1.59823	$P_4\text{-}O_{16}$	1.57227
$O_1\text{-}P_1\text{-}O_2$	110.915	$O_5\text{-}P_2\text{-}O_6$	111.109	$O_9\text{-}P_3\text{-}O_{10}$	113.086	$O_{13}\text{-}P_3\text{-}O_{14}$	112.316
$O_1\text{-}P_1\text{-}O_3$	110.496	$O_5\text{-}P_2\text{-}O_7$	109.775	$O_9\text{-}P_3\text{-}O_{11}$	109.079	$O_{13}\text{-}P_3\text{-}O_{15}$	110.363
$O_1\text{-}P_1\text{-}O_4$	104.242	$O_5\text{-}P_2\text{-}O_8$	110.583	$O_9\text{-}P_3\text{-}O_{12}$	111.975	$O_{13}\text{-}P_3\text{-}O_{16}$	102.628
$O_2\text{-}P_1\text{-}O_3$	110.021	$O_6\text{-}P_2\text{-}O_7$	109.648	$O_{10}\text{-}P_3\text{-}O_{11}$	106.218	$O_{14}\text{-}P_3\text{-}O_{15}$	108.520
$O_2\text{-}P_1\text{-}O_4$	116.488	$O_6\text{-}P_2\text{-}O_8$	107.985	$O_{10}\text{-}P_3\text{-}O_{12}$	106.946	$O_{14}\text{-}P_3\text{-}O_{16}$	113.200
$O_3\text{-}P_1\text{-}O_4$	104.351	$O_7\text{-}P_2\text{-}O_8$	107.659	$O_{11}\text{-}P_3\text{-}O_{12}$	109.326	$O_{15}\text{-}P_3\text{-}O_{16}$	109.718

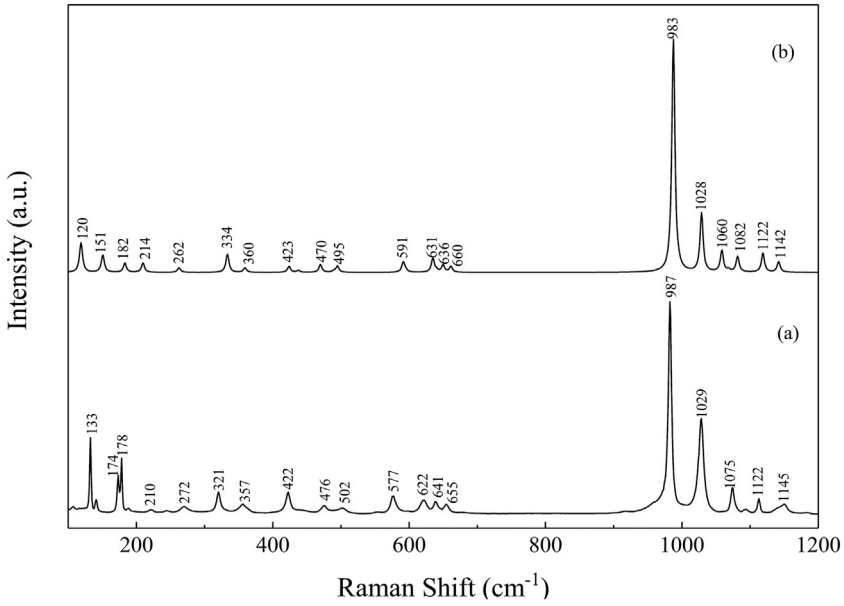

Fig. 3. Experimental (a) and calculated (b) Raman spectra of $Mg_3(PO_4)_2$-I. The calculated Raman spectrum of $Mg_3(PO_4)_2$-I is normalized for comparison with experimental values, and the Lorentzian smearing is 7 cm^{-1}.

observed peaks at 622, 641 and 655 cm^{-1} correspond to the bands calculated at 631, 636 and 660 cm^{-1}, which are associated to the ν_4 out of plane bending modes of the PO_4 units. The bands in the region 600–700 cm^{-1} were not assigned by Termine and Lundy [18]. One low intensity Raman band of ν_2 in-plane bending mode at 591 cm^{-1} is calculated which is located in the experimental spectrum at 577 cm^{-1}, the assignment of this band does not match the literature data [18]. In the measured and calculated Raman spectra, the peaks in the range of 240 to 510 cm^{-1} are assigned to Mg—O bending modes. The frequencies of these bands below 240 cm^{-1} are defined as lattice vibrations. The division of spectrum based on to the vibrational mode images was shown in Fig. S1 of the Supplementary Information. Actually, the assignations of these vibrational modes are not same as vibrational modes of $Pb_3(PO_4)_2$ [41]. According to the cell parameters of $Pb_3(PO_4)_2$ [42], the shifts of vibrational modes can be explained by two reasons. On the one hand, the symmetry of PO_4 tetrahedra in $Pb_3(PO_4)_2$ and $Mg_3(PO_4)_2$-I are different. On the other hand, the impact of Pb atoms on PO_4 tetrahedra is weak, while Mg atoms extremely distorts the PO_4 tetrahedra in $Mg_3(PO_4)_2$-I.

Fig. 4 shows the experimental and calculated Raman spectra of $Mg_3(PO_4)_2$-II. 17 Raman vibrational modes are observed for $Mg_3(PO_4)_2$-II. Two peaks observed at 1071 and 1103 cm^{-1} are assigned to ν_3 antisymmetric stretching mode, whereas they site at 1071 and 1111 cm^{-1} in calculated Raman spectrum. In theoretical and experimental spectra, the most intense bonds both site at 992 cm^{-1}, and the second most intense bonds sites at 931 cm^{-1} and 916 cm^{-1}, respectively. It is noted that a lower intensity peak appears at the left shoulder of the second most intense peak in both the experimental and calculated Raman spectra. This

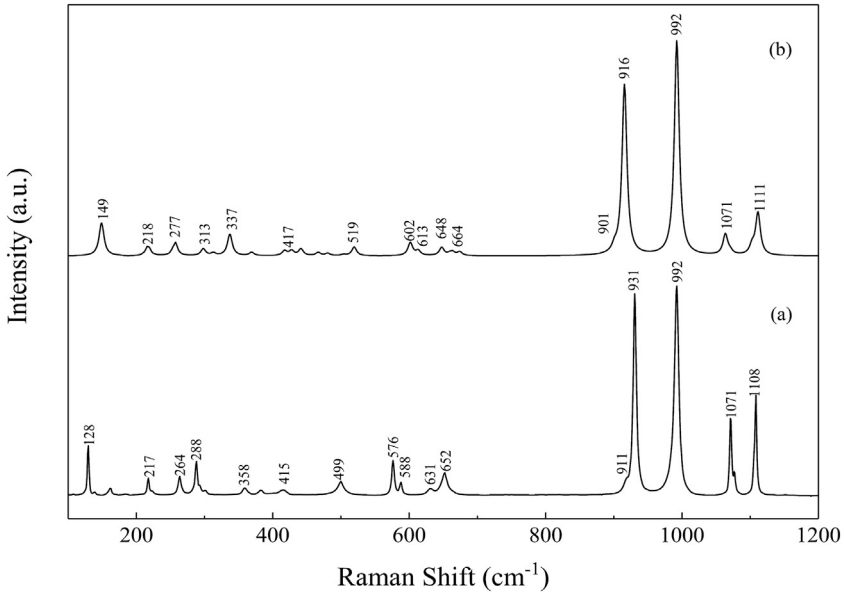

Fig. 4. Experimental (a) and calculated (b) Raman spectra of $Mg_3(PO_4)_2$-II. The calculated Raman spectrum of $Mg_3(PO_4)_2$-II is normalized for comparison with experimental values, and the Lorentzian smearing is 8 cm^{-1}.

Table 4
The experimental and calculated Raman shift of $Mg_3(PO_4)_2$-I and $Mg_3(PO_4)_2$-II.

$Mg_3(PO_4)_2$-I				$Mg_3(PO_4)_2$-II			
ν_{exp} (cm^{-1})	ν_{cal} (cm^{-1})	Symm	Vibrational modes	ν_{exp} (cm^{-1})	ν_{cal} (cm^{-1})	Symm	Vibrational modes
133	120	A_g	Lattice vibration	129	149	A_g	Lattice vibration
174	151	A_g	Lattice vibration	217	218	A_g	Lattice vibration
178	182	A_g	Lattice vibration	264	277	A_g	Mg-O bending
210	214	B_g	Lattice vibration	288	313	B_g	Mg-O bending
272	262	A_g	Mg-O bending	358	337	A_g	Mg-O bending
321	334	A_g	Mg-O bending	415	417	B_g	Mg-O bending
357	360	A_g	Mg-O bending		441	A_g	Mg-O bending
422	423	A_g	Mg-O bending	499	519	B_g	Mg-O bending
476	470	A_g	Mg-O bending	576	602	A_g	ν_2
502	495	B_g	Mg-O bending	588	613	B_g	ν_2
577	591	A_g	ν_2	631	648	A_g	ν_4
622	631	A_g	ν_4	652	664	A_g	ν_4
641	636	A_g	ν_4	911	901	B_g	ν_1
655	660	B_g	ν_4	931	916	A_g	ν_1
987	983.	A_g	ν_1	992	992	B_g	ν_1
1029	1028	B_g	ν_1	1071	1071	B_g	ν_3
	1060	A_g	ν_3	1108	1111	A_g	ν_3
1075	1082	A_g	ν_3				
1122	1122	B_g	ν_3				
1145	1142	B_g	ν_3				

peak is owing to the splitting of the vibrational mode owing to the P—O_2 bond longer than other P—O bonds [43]. The two most intense vibrational modes and this splitting vibrational mode are assigned to ν_1 symmetric stretching mode. The other Raman spectrum of $Mg_3(PO_4)_2$-II can be divided in four regions, 620–700 cm^{-1}, 550–620 cm^{-1}, 240–550 cm^{-1} and 120–240 cm^{-1}. This division of spectrum is in good agreement with $Mg_3(PO_4)_2$-I. The detail calculation data of the vibrational modes of $Mg_3(PO_4)_2$-II are in Support Information. The experimental and calculated Raman shift of $Mg_3(PO_4)_2$-I and $Mg_3(PO_4)_2$-II with assignments derived from the simulated are listed in Table 4.

The calculated Raman spectrum of $Mg_3(PO_4)_2$-III precisely reproduces the experimental measurement (Fig. 5). With four distinct PO_4 tetrahedra, the Raman spectra of $Mg_3(PO_4)_2$-III is more complicated than $Mg_3(PO_4)_2$-I, II. It is difficult to discern every vibration in detail based on the experimental data alone. However, combined with the calculation results, each vibrational mode can be assigned. In the region of 900–990 cm^{-1}, four intense peaks are observed at 951, 968, 978 and 997 cm^{-1} in experimental spectrum and at 933, 951, 972 and 996 cm^{-1} in the calculated spectrum. The first two bands are attributed to ν_1 symmetric stretching of $P(3)O_4$ tetrahedra, and the next band is indexed to ν_1 symmetric stretching of $P(4)O_4$ tetrahedra. Similarly, the most intense peak is indexed to symmetric stretching of $P(2)O_4$ tetrahedra. Two experimental bands observed at 1006 and 1019 cm^{-1} and the corresponding calculated bonds at 1000 and 1031 cm^{-1} appear to be combination bands: $\nu_1 + \nu_3$. The first mode is contributed by ν_3 of P(1)O_4 tetrahedra and ν_1 of $P(3)O_4$ tetrahedra, while the second mode is contributed by ν_1 of P(1)O_4 tetrahedra and ν_3 of $P(3)O_4$ tetrahedra. The bands observed in the region of ν_3 have Raman shift of 1031, 1055, 1060, 1084, 1117 and 1158 cm^{-1}, the corresponding modes are located at 1041, 1048, 1063, 1086, 1117 and 1165 cm^{-1}. Compared to ν_1, all ν_3 are related to three types of P atoms. The bending modes of PO_4 tetrahedra of $Mg_3(PO_4)_2$-III appear in the range of 550–670 cm^{-1}. In the calculated spectrum, these bonds are located at 569, 592, 616, 633, 644 and 670 cm^{-1}, and in their experimental spectrum, these

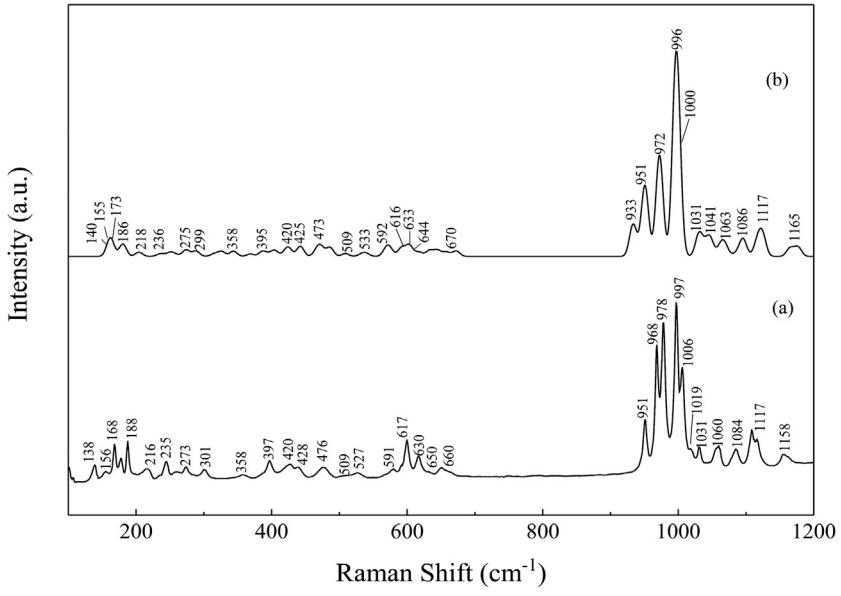

Fig. 5. Experimental (a) and calculated (b) Raman spectra of $Mg_3(PO_4)_2$-III. The calculated Raman spectrum of $Mg_3(PO_4)_2$-III is normalized for comparison with experimental values, and the Lorentzian smearing is 8 cm^{-1}.

corresponding bonds are observed at 574, 591, 617, 630,650 and 660 cm^{-1}. It should be noted that the bands at 574, 591 and 617 are assigned to the bending of P(1,2,4)O_4 tetrahedra. In the experimental spectrum, seven Mg—O vibrational modes are observed at 358, 397, 420, 428, 476, 509 and 527 cm^{-1} and theoretically computed wavenumbers are 358, 395, 420, 425, 473, 509 and 533 cm^{-1}. The details of assignation of modes of $Mg_3(PO_4)_2$-III are given in Table 5.

3.3. General discussion

The comparison of Figs. 3–5 reveals spectral feature in the Raman spectra that distinguish $Mg_3(PO_4)_2$-I, II, III. According to Table 1, the distortion of the PO_4 tetrahedra is higher in $Mg_3(PO_4)_2$-II than in $Mg_3(PO_4)_2$-I. These are also expressed in the Figs. 3 and 4 as broader ν_1 peaks in $Mg_3(PO_4)_2$-II than in $Mg_3(PO_4)_2$-I. Similarly, fewer vibrational peaks in Figs. 3 and 4 than in Fig. 5 indicate the degeneration of Mg—O polyhedrons and PO_4 tetrahedra. According to vibrational images in Appendix B of Support Information, it should be note that only Mg (1) atoms are involved in the vibrations of $Mg_3(PO_4)_2$-I, only Mg (2) atoms are involved in the vibrations of $Mg_3(PO_4)_2$-II. However, the vibrations of $Mg_3(PO_4)_2$-III rely on the movements of six distinct magnesium atoms. Moreover, the vibrations of PO_4 tetrahedra of $Mg_3(PO_4)_2$-III are contributed by atomistic processes of movements of four nonequivalent P atoms.

It is interesting to note that the phase transition among three polymorphs pose an importance effects on intensity and frequency of the analogous vibrational mode. More importantly, changes in the intensity of vibrational mode will impact the physical and chemical properties of the crystal. In fact, the Raman intensity is determined by p-th mode at the center of the first Brillouin zone (Γ point):

$$I_R \propto \left(\frac{\partial \alpha_R}{\partial Q_p}\right)^2.$$

where Raman mode Q_p due to the α_R component of the polarizability tensor.

Because the polarizability tensor of the stretching vibration of PO_4 tetrahedra larger than the bending vibration, it is very probable that the stretching modes more intense than bending modes, as shown in Figs. 3–5. In fact, the effects of lattice on vibrational properties can be investigated by analyzing analogous vibrational modes. There are three typical modes denoted as ν_{B1}-ν_{B3} located at 636, 648 and 633 cm^{-1} are shown in Fig. 6. P—O bending vibrational modes ν_{B1}, ν_{B2}, ν_{B3} belonged to $Mg_3(PO_4)_2$-I, II, III, respectively. According to Table 1, because the error of average bond angles of $Mg_3(PO_4)_2$-I, II, III are less than 2‰, which makes the intensity and frequency of these three bending vibrations have close values. This shows that the effects of phase transition on the bending vibrational properties of $Mg_3(PO_4)_2$ are not

Table 5
The experimental and calculated Raman shift of $Mg_3(PO_4)_2$-III.

Raman shift			
ν_{exp} (cm^{-1})	ν_{cal} (cm^{-1})	Vibrational modes	Involved characteristic atoms
138	140	Lattice vibration	–
156	155	Lattice vibration	–
168	173	Lattice vibration	–
177	180	Lattice vibration	–
188	186	Lattice vibration	–
200	191	Lattice vibration	–
216	218	Lattice vibration	–
235	236	Lattice vibration	–
244	248	Lattice vibration	–
259	260	Lattice vibration	–
273	275	Lattice vibration	–
301	299	Lattice vibration	–
345	344	Lattice vibration	–
358	358	Mg-O bending	Mg(1–3, 5)
397	395	Mg-O bending	Mg(1–6)
420	420	Mg-O bending	Mg(1–4, 6)
428	425	Mg-O bending	Mg(1–6)
476	473	Mg-O bending	Mg(1, 4)
509	509	Mg-O bending	Mg(3)
527	533	Mg-O bending	Mg(1, 4)
574	569	ν_2	P(1, 2, 4)
591	592	ν_2	P(1, 2, 4)
617	616	ν_2	P(1, 2, 4)
630	633	ν_4	P(1, 2)
650	644	ν_4	P(2, 3)
660	670	ν_4	P(3)
951	933	ν_1	P(3)
968	951	ν_1	P(3)
978	972	ν_1	P(4)
997	996	ν_1	P(2)
1006	1000	$\nu_1 + \nu_3$	P(1, 3)
1019	1031	$\nu_1 + \nu_3$	P(1, 3)
1031	1041	ν_3	P(1–4)
1055	1048	ν_3	P(1, 2, 4)
1060	1063	ν_3	P(1–4)
1084	1086	ν_3	P(1–4)
1117	1117	ν_3	P(1, 4)
1158	1165	ν_3	P(1, 3)

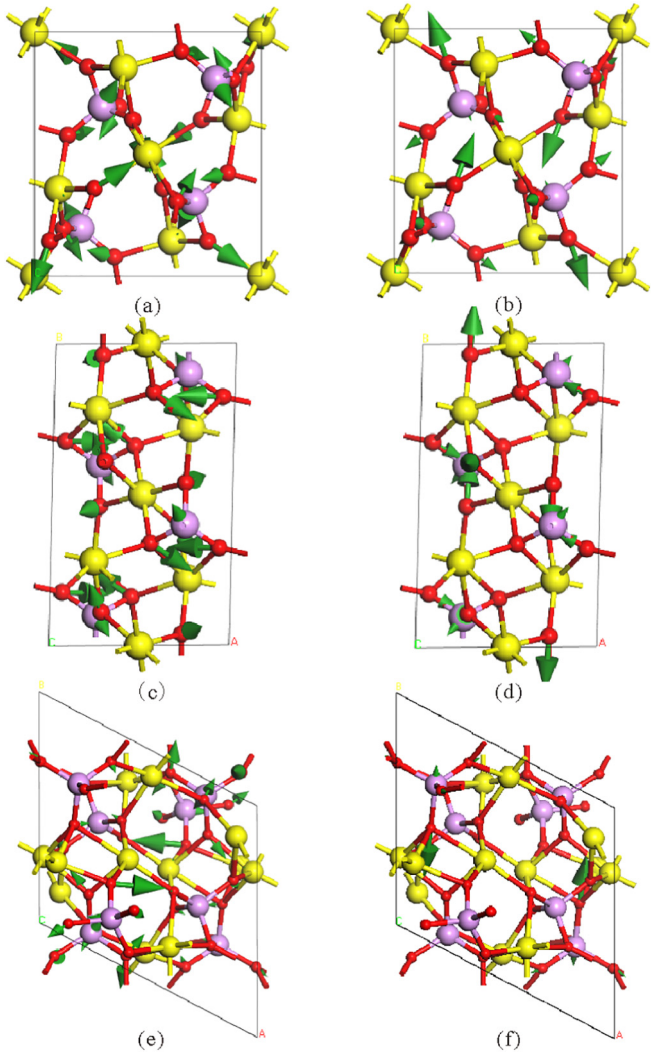

Fig. 6. Analogous modes of $Mg_3(PO_4)_2$. (a) mode located at 636 cm^{-1} in $Mg_3(PO_4)_2$-I. (b) mode located at 987 cm^{-1} in $Mg_3(PO_4)_2$-I. (c) mode located at 648 cm^{-1} in $Mg_3(PO_4)_2$-II. (d) mode located at 992 cm^{-1} in $Mg_3(PO_4)_2$-II. (e) mode located at 633 cm^{-1} in $Mg_3(PO_4)_2$-III. (f) mode located at 996 cm^{-1} in $Mg_3(PO_4)_2$-III.

significant. Similarly, three typical symmetrical stretching modes denoted as ν_{S1}, ν_{S2}, ν_{S3} located at 987, 992 and 996 cm^{-1} are also shown in Fig. 5. These three vibrational modes belong to $Mg_3(PO_4)_2$-I, II, III, respectively. For the stretching vibration of phosphate, the changes of its polarizability are mainly determined by the bond length except the p-th mode. The intensity of ν_{S1} and ν_{S2} is higher than other symmetrical stretching modes of $Mg_3(PO_4)_2$-I, II. However, the intensity of ν_{S3} is lower than ν_{S1} and ν_{S2}. The main reason is the local crystalline site field in $Mg_3(PO_4)_2$-III limits the vibration of $P(3)O_4$ tetrahedra.

According to the calculations, δ_s (scissoring vibration) of PO_4 tetrahedra in $Mg_3(PO_4)_2$-I, II, III are listed in Fig. 7. It should be noted that δ_s in $Mg_3(PO_4)_2$-I, II evolves into two types of modes, which are located at 592 and 616 cm^{-1} in $Mg_3(PO_4)_2$-III. Although these two δ_s are depends on the vibrations of $P(1,2,4)O_4$ tetrahedra, it is obvious that $P(2)O_4$ tetrahedra dominates the first δ_s and $P(1)O_4$ tetrahedra dominates the other. Compared with $P(1)O_4$ tetrahedra, the δ_s dominated by $P(2)O_4$ tetrahedra have a low Raman intensity and the δ_s dominated by P(3) or P(4) do not have Raman activity. The frequencies of δ_s in $Mg_3(PO_4)_2$-I, II, III are close, which mean the strengths of P—O bonds in $Mg_3(PO_4)_2$-I, II, III are almost consistent. The difference between Raman intensities implies that the interactions of phonon of $Mg_3(PO_4)_2$-III are significantly different from the other two polymorphs.

4. Conclusions

In this work, the vibrational properties of three $Mg_3(PO_4)_2$ polymorphs have been investigated by means of experimental measurements and density functional theoretical calculations. According to the calculated results, the Raman-active modes of $Mg_3(PO_4)_2$-I, II, III have been assigned. Some bands can be used as "fingerprint" to identify these compounds, such as 422, 577, 983 and 1208 cm^{-1} in the Raman spectrum of $Mg_3(PO_4)_2$-I, 415, 652, 911 and 931 cm^{-1} in the Raman spectrum of $Mg_3(PO_4)_2$-II, 420, 476, 617, 997 and 1117 cm^{-1} in the Raman spectrum of $Mg_3(PO_4)_2$-III.

The agreement between the experimental and calculated spectra is excellent, which makes it possible to accurately investigate the effect of structural transformations on vibrational properties of three $Mg_3(PO_4)_2$ polymorphs. Raman spectra of $Mg_3(PO_4)_2$-I and $Mg_3(PO_4)_2$-II are generally similar due to their same chemical composition and space group. By comparing the crystal structures, the reason for the difference in Raman spectra in the high-frequencies part of the spectrum (900–1200 cm^{-1}) is due to the discrepancy in the lengths of P—O bonds. In the low-frequencies part of spectrum (100–500 cm^{-1}), the decreasing of symmetry leads to more peaks appearing on the Raman spectrum of $Mg_3(PO_4)_2$-III. The structural transformation enhances the phonon interactions of $Mg_3(PO_4)_2$-III, by investigating the δ_s in three $Mg_3(PO_4)_2$-I, II, III, which might lead to the thermal property of $Mg_3(PO_4)_2$-III different from $Mg_3(PO_4)_2$-I and $Mg_3(PO_4)_2$-II. Some bonds strength of P—O in $Mg_3(PO_4)_2$-II, III are weaker than in $Mg_3(PO_4)_2$-I as expressed by the frequency of first ν_1. Similarly, low intensity of ν_{S3} indicate bond strength of P—O in $Mg_3(PO_4)_2$-III is weaker than in $Mg_3(PO_4)_2$-I, II.

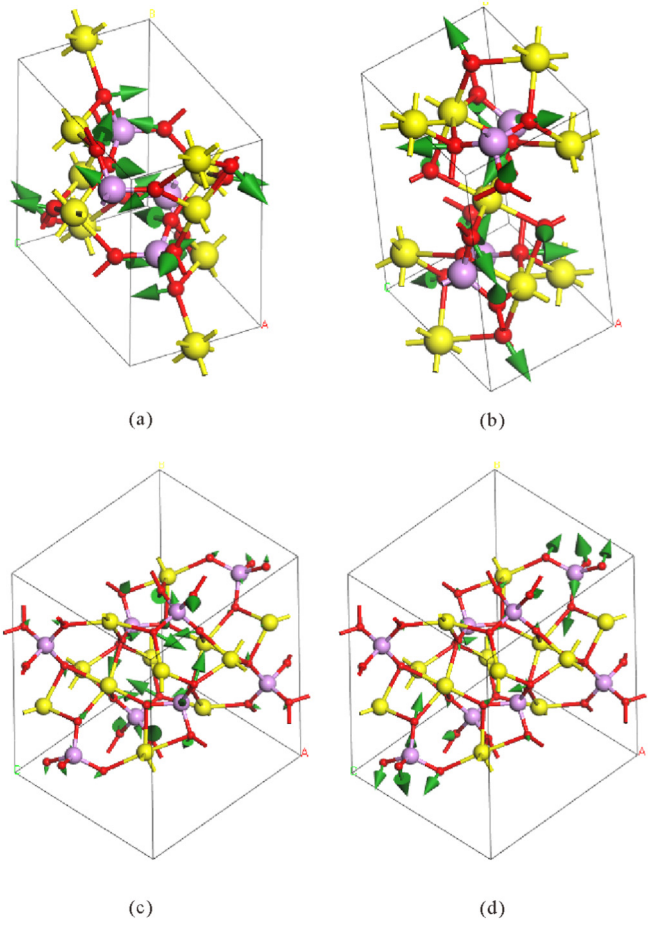

Fig. 7. δ_s in $Mg_3(PO_4)_2$. (a) mode located at 591 cm^{-1} in $Mg_3(PO_4)_2$-I. (b) mode located at 602 cm^{-1} in $Mg_3(PO_4)_2$-II. (c) mode located at 592 cm^{-1} in $Mg_3(PO_4)_2$-III. (d) mode located at 616 cm^{-1} in $Mg_3(PO_4)_2$-III.

CRediT authorship contribution statement

Xin Hu: Methodology, Investigation, Data curation, Writing. **Lei Liu**: Data curation. **Shuangmeng Zhai**: Conceptualization, Supervision, Funding acquisition.

Declaration of competing interest

The authors declare no competing financial interest.

Acknowledgements

The authors thank Dr. R. Wang for helpful discussion. We are grateful to two anonymous reviewers for their helpful comments and suggestion. This work was financially supported by Strategic Priority Research Program of Chinese Academy of Sciences (Grant No. XDB 41000000) and the Guizhou Science and Technology Department (Grant No. [2016] 1157).

Supplementary data

Supplementary information to this article can be found. The atomic positions of optimized $Mg_3(PO_4)_2$-I, II, III are given in Tables S1 and S2. The vibrational modes of $Mg_3(PO_4)_2$-I, II, III are given in Figs. S1, S2 and S3, respectively. Supplementary data to this article can be found online at https://doi.org/10.1016/j.saa.2020.118906.

References

[1] A.G. Nord, P. Kierkegaard, The crystal structure of $Mg_3(PO_4)_2$, Acta Chem. Scand. 22 (1968) 1466–1474.
[2] F. Brunet, D. Vielzeuf, The farringtonite/$Mg_3(PO_4)_2$-II transformation: a new curve for pressure calibration in piston-cylinder apparatus, Eur. J. Mineral. 8 (2) (1996) 349–354.
[3] H. Annersten, A.G. Nord, High-pressure phase of magnesium orthophosphate, Acta Chem. Scand. A34 (1980) 389–390.
[4] F. Brunet, C. Chopin, A. Elfakir, M. Quarton, Crystal and powder XRD data of $Mg_3(PO_4)_2$-III: high-temperature and high-pressure form, Powder Diffract. 10 (4) (1995) 293–295.
[5] S. Jaulmes, A. Elfakir, M. Quarton, F. Brunet, C. Chopin, Structure cristalline de la phase haute température et haute pression de $Mg_3(PO_4)_2$, J. Solid State Chem. 129 (2) (1997) 341–345.

[6] F. Brunet, C. Chopin, F. Seifert, Phase relations in the MgO-P_2O_5-H_2O system and the stability of phosphoellenbergerite: petrological implications, Contrib. Mineral. Petr. 131 (1) (1998) 54–70.
[7] E.R. DuFresne, S.K. Roy, A new phosphate mineral from the springwater pallasite, Geochim. Cosmochim. Acta 24 (3–4) (1961) 198–205.
[8] P. Carmona, J. Bellanato, E. Escolar, Infrared and Raman spectroscopy of urinary calculi: a review, Biospectroscopy 3 (5) (1997) 331–346.
[9] T. Ceyhan, V. Günay, A. Çapoğlu, H. Sayrak, C. Karaca, Production and characterization of a glass-ceramic biomaterial and in vitro and in vivo evaluation of its biological effects, Acta Orthop. Traumato. 41 (4) (2007) 307–313.
[10] O. Kaygili, C. Tatar, F. Yakuphanoglu, Structural and dielectrical properties of Mg_3-$Ca_3(PO_4)_2$ bioceramics obtained from hydroxyapatite by sol-gel method, Ceram. Int. 38 (7) (2012) 5713–5722.
[11] E. Vorndran, K. Wunder, C. Moseke, I. Biermann, F.A. Müller, K. Zorn, U. Gbureck, Hydraulic setting $Mg_3(PO_4)_2$ powders for 3D printing technology, Adv. Appl. Ceram. 110 (8) (2011) 476–481.
[12] Y. Xin, C. Liu, X. Zhang, G. Tang, X. Tian, P.K. Chu, Corrosion behavior of biomedical AZ91 magnesium alloy in simulated body fluids, J. Mater. Res. 22 (7) (2007) 2004–2011.
[13] N.B. Shul'ga, V.V. Samusevich, Lead (II) sorption by magnesium phosphates, Russ. J. Appl. Chem. 75 (3) (2002) 378–384.
[14] H. Huang, J. Liu, S. Wang, Y. Jiang, D. Xiao, L. Ding, F. Gao, Nutrients removal from swine wastewater by struvite precipitation recycling technology with the use of $Mg_3(PO_4)_2$ as active component, Ecol. Eng. 92 (2016) 111–118.
[15] J. Eom, J. Cho, $Mg_3(PO_4)_2$-nanoparticle-coated $LiCoO_2$ vs $LiCo_{0.96}M_{0.04}O_2$ (M= Mg and Zn) on electrochemical and storage characteristics, J. Electrochem. Soc. 155 (3) (2008) A201–A205.
[16] Y. Wang, Y. Zhou, C. Su, N. Tong, Z. Han, F. Liu, Effects of $Mg_3(PO_4)_2$ addition on the crystal structure, mechanical and thermophysical properties of $CaZr_4P_6O_{24}$ ceramics, J. Alloy. Compd. 806 (2019) 302–309.
[17] J.C. Joubert, E.F. Bertaut, Vacancies ordering in new metastable orthophosphates $(Co_3)P_2O_8$ and $(Mg_3)P_2O_8$ with olivine-related structure, Z. Kristallogr. Cryst. Mater. 136 (1–6) (1972) 98–105.
[18] L.H. Fuchs, E. Olsen, E. Gebert, New X-ray and compositional data for farringtonite, $Mg_3(PO_4)_2$, Am. Mineral. 58 (9–10) (1973) 949–951.
[19] A. Baykal, M. Kizilyalli, R. Kniep, Synthesis and characterization of anhydrous magnesium phosphate $Mg_3(PO_4)$, Turk. J. Chem. 21 (4) (1997) 394–400.
[20] J.D. Termine, D.R. Lundy, Vibrational spectra of some phosphate salts amorphous to X-ray diffraction, Calcif. Tissue. Res. 15 (1) (1974) 55–70.
[21] X.L. Tang, D.X. Feng, S.M. Wan, L. Kang, B. Zhang, Z.S. Lin, Crystal structure and Raman spectrum of $Ba_2Pb(B_3O_6)_2$, Mater. Chem. Phys. 163 (2015) 501–506.
[22] F. Colmenero, L.J. Bonales, J. Cobos, V. Timón, Density functional theory study of the thermodynamic and Raman vibrational properties of γ-UO_3 polymorph, J. Phys. Chem. C 121 (27) (2017) 14507–14516.
[23] M.B. Smirnov, E.M. Roginskii, K.S. Smirnov, R. Baddour-Hadjean, J.P. Pereira-Ramos, Unraveling the structure–Raman spectra relationships in V_2O_5 polymorphs via a comprehensive experimental and DFT study, Inorg. Chem. 57 (15) (2018) 9190–9204 2018.
[24] B.H. Toby, EXPGUI, a graphical user interface for GSAS, J. Appl. Crystallogr. 34 (2) (2001) 210–213.
[25] A.C. Larson, R.B. Von Dreele, Los Alamos Natl. Lab. Rep, LAUR, 2004 86–748.
[26] M.D. Segall, P.J. Lindan, M.A. Probert, C.J. Pickard, P.J. Hasnip, S.J. Clark, First-principles simulation: ideas, illustrations and the CASTEP code, J. Phys. Condens. Matter 14 (11) (2002) 2717.
[27] S. Baroni, S. De Gironcoli, A.D. Corso, P. Giannozzi, Phonons and related crystal properties from density-functional perturbation theory, Rev. Mod. Phys. 73 (2) (2001) 515.
[28] X. Gonze, C. Lee, Dynamical matrices, born effective charges, dielectric permittivity tensors, and interatomic force constants from density-functional perturbation theory, Phys. Rev. B 55 (16) (1997) 10355.
[29] K. Refson, P.R. Tulip, S.J. Clark, Variational density-functional perturbation theory for dielectrics and lattice dynamics, Phys. Rev. B 73 (15) (2006) 155114.
[30] V. Milman, K. Refson, S.J. Clark, C.J. Pickard, M.D. Segall, Electron and vibrational spectroscopies using DFT, plane waves and pseudopotentials: CASTEP implementation, J. Mol. Struc-THEOCHEM. 954 (1–3) (2010) 22–35.
[31] D.M. Ceperley, B.J. Alder, Ground state of the electron gas by a stochastic method, Phys. Rev. Lett. 45 (7) (1980) 566.
[32] J.P. Perdew, K. Burke, M. Ernzerhof, Generalized gradient approximation made simple, Phys. Rev. Lett. 77 (18) (1996) 3865.
[33] D.R. Hamann, M. Schlüter, C. Chiang, Norm-conserving pseudopotentials, Phys. Rev. Lett. 43 (20) (1979) 1494.
[34] N. Troullier, J.L. Martins, Efficient pseudopotentials for plane-wave calculations, Phys. Rev. B 43 (3) (1991) 1993.
[35] M.C. Payne, M.P. Teter, D.C. Allan, T.A. Arias, J.D. Joannopoulos, Iterative minimization techniques for ab initio total-energy calculations: molecular dynamics and conjugate gradients, Rev. Mod. Phys. 64 (4) (1992) 1045.
[36] B.G. Pfrommer, M. Côté, S.G. Louie, M.L. Cohen, Relaxation of crystals with the quasi-Newton method, J. Comput. Phys. 131 (1) (1997) 233–240.
[37] J. Wang, J. You, M. Wang, L. Lu, S. Wan, A. Sobol, In-situ studies on the microstructure evolution of $A_2W_2O_7$ (A = Li, Na, K) during melting by high temperature Raman spectroscopy and density functional theory, Spectrochim. Acta A. 185 (2017) 188–196.
[38] N. Ma, J. You, L. Lu, J. Wang, M. Wang, S. Wan, Micro-structure studies of the molten binary K_3AlF_6-Al_2O_3 system by in situ high temperature Raman spectroscopy and theoretical simulation, Inorg. Chem. Front. 5 (8) (2018) 1861–1868.
[39] S. Zhang, S. Wan, Y. Zeng, S. Jiang, X. Gong, J. You, In situ Raman spectroscopy and DFT studies of the Li_2GeO_3 melt structure, Inorg. Chem. 58 (8) (2019) 5025–5030.
[40] M.I. Aroyo, A. Kirov, C. Capillas, J.M. Perez-Mato, H. Wondratschek, Bilbao crystallographic server. II. Representations of crystallographic point groups and space groups, Acta Crystallogr. A 62 (2) (2006) 115–128.
[41] B. Mihailova, U. Bismayer, A. Engelhardt, B. Güttler, Wall-related Raman scattering in ferroelastic lead phosphate $Pb_3(PO_4)_2$, J. Phys. Condens. Matter 13 (41) (2001) 9383–9392.
[42] R.J. Angel, U. Bismayer, W.G. Marshall, Local and long-range order in ferroelastic lead phosphate at high pressure, Acta Crystallogr. B 60 (1) (2004) 1–9.
[43] L. Popović, D.D. Waal, J.C.A. Boeyens, Correlation between Raman wavenumbers and P-O bond lengths in crystalline inorganic phosphates, J. Raman Spectrosc. 36 (1) (2005) 2–11.